Sustainable Energy & Fuels

PAPER

View Article Online
View Journal | View Issue



Cite this: *Sustainable Energy Fuels*, 2022, **6**, 2358

# Extended oligo-cyclopentadithiophene dyes for liquid and solid-state dye-sensitised solar cells†

Artit Jarusarunchai,[a] Xuan Liu,[b] Wenjun Wu [b] and Neil Robertson *[a]

A new series of dyes called **T-CPDT**, without a strong electron-donor moiety, was designed, based on a combination of previously-reported **CPDT** and **5T** dyes, and synthesised. By addition of a thiophene unit between alkylated CPDT unit(s) and the cyanoacrylic acid acceptor group, their optical, electrochemical and photovoltaic properties were tuned and studied. Upon extending CPDT units from 1 to 3, hence, **T-CPDT-1**, **T-CPDT-2** and **T-CPDT-3**, the UV-Vis absorption undergoes a bathochromic shift together with a larger extinction coefficient, while the first oxidation potential is less positive. These dyes were applied in DSSC devices with $I^-/I_3^-$ electrolyte and with a Spiro-OMeTAD hole transporter. Among the **T-CPDT** series, **T-CPDT-3** shows the highest PCE of 5.88% with $I^-/I_3^-$ electrolyte and 4.38% for a solid-state device, mainly due to larger $J_{sc}$ and $V_{oc}$. Their photovoltaic results with $I^-/I_3^-$ electrolyte were compared to those of **CPDT-3** and **5T** under the same conditions. We also show that the addition of the extra thiophene to **CPDT-3**, forming **T-CPDT-3**, leads to slower electron recombination kinetics, compared to those of **CPDT-3** and **5T**. Interestingly, the solid-state device with **T-CPDT-3** achieves a very high $J_{sc}$ of 11.27 mA cm$^{-2}$ with a less than 1 micron thick $TiO_2$ film which is unusually thin for solid-state devices.

Received 28th January 2022
Accepted 31st March 2022

DOI: 10.1039/d2se00131d

rsc.li/sustainable-energy



## Introduction

It has been around 30 years since dye-sensitised solar cells (DSSCs) emerged as a promising photovoltaic technology following the seminal report of efficient DSSCs by O'Regan and Grätzel.[1] The working principle of DSSCs is closely related to photosynthesis by utilisation of dye molecules as a photo-absorber to generate electrons, which are subsequently transferred to a mesoporous semiconductor, mostly $TiO_2$. There are three main classes of dyes that have been studied, namely Ru-polypyridyl complexes, Zn-porphyrin complexes and metal-free organic dyes.[2] Out of these, metal-free organic dyes have been researched extensively due to their high extinction coefficient, availability of starting materials, flexible design and ease of tuning their electronic properties. These features enable compatibility with different types of DSSC architecture.[2–5] The conventional metal-free organic dyes are designed based on the state-of-the-art donor–π–acceptor (D–π–A) structure. In this design, modification of the donors, π-conjugated spacers and acceptors plays the key role in tuning the dyes' electronic and electrochemical properties and thus, performance of DSSCs.

In addition to the conventional motif, an additional donor or acceptor group has also been introduced into the D–π–A structure, yielding 2D–π–A or D–A′–π–A, respectively, in order to broaden and shift the absorption toward the red region.[6,7] In addition, the π-conjugated spacers can also be modified to expand the absorption spectrum. There are three approaches that can be used to engineer the π-conjugated spacers: (1) variation of the spacer length to adjust the HOMO–LUMO gap; (2) change in the types of the spacers as the absorption is characteristic of the spacers; and (3) modification of the planarity of the spacers.[8] The commonly used spacers are thiophene and its derivatives as they provide good π-conjugation and planarity.[9] Since the planarity can be used to determine the degree of extended effective π-conjugation length, bridging the two neighbouring rings is used to maximise the planarity.[8] In this case, 4*H*-cyclopenta[2,1-*b*:3,4-*b*′]dithiophene (CPDT) possesses more rigid conjugation and co-planarity, providing a higher absorption coefficient as well as electron-donating ability.[10,11] Apart from that, CPDT also provides facile introduction of long alkyl chains which can help to prevent aggregation and prevent electron recombination.[11–13]

In contrast to the conventional D–π–A, Abate *et al.* removed the strong donor group carbazole of the **MK-2** dye to obtain the **5T** dye (Fig. 1), resulting in increased efficiency due to exclusively higher $V_{oc}$ in solid-state DSSCs (ssDSSCs) for **5T** compared

[a]*School of Chemistry, University of Edinburgh, King's Buildings, David Brewster Road, Edinburgh, EH9 3FJ, UK. E-mail: Neil.Robertson@ed.ac.uk*

[b]*Key Laboratory for Advanced Materials and Feringa Nobel Prize Scientist, Joint Research Center Shanghai Key Laboratory of Functional Materials Chemistry, School of Chemistry and Molecular Engineering, East China University of Science & Technology, 130 Meilon Road, Shanghai 200237, P. R. China. E-mail: wjwu@ecust.edu.cn*

† Electronic supplementary information (ESI) available: Details of dye syntheses, experimental and theoretical dye characterisation, cell fabrication in liquid electrolyte and solid HTM and characterisation. See DOI: 10.1039/d2se00131d

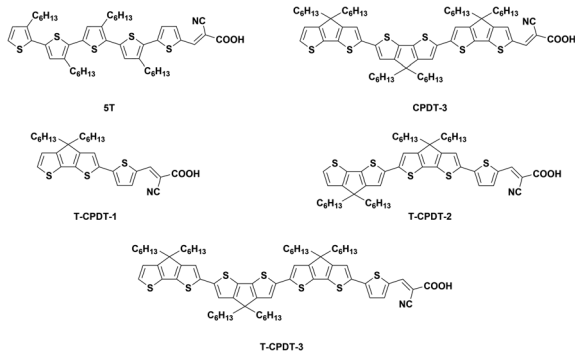


Fig. 1 The molecular structures of the 5T, CPDT-3 and T-CPDT series.

with **MK-2**.[14] This study paved the way for a new strategy of dye design by omitting the strong donor moiety, but, instead, using the π-spacer as both donor and π-conjugation parts. In the ensuing year, a new series of dyes called **CPDT** (Fig. S1†) was designed and synthesised by using CPDT as the π-spacer.[15] The coplanarity within CPDT units led to a bathochromic shift of $\lambda_{max}$ and higher extinction coefficients with increasing CPDT units, compared with the twisted structure of **5T** due to larger dihedral angles between thiophene units. The efficiency of the devices based on the **CPDT** series and **5T** was compared in liquid and solid-state DSSCs. The results showed that the **CPDT-3** dyes (Fig. 1) achieved higher $J_{sc}$ in both types of cells, especially in ssDSSC, but gave lower $V_{oc}$ than **5T**, which was mainly due to recombination.

As seen from the **5T** structure which has a thiophene unit attached directly to the cyanoacrylic acid, we hypothesise that a similar configuration may help the **CPDT** series to gain higher $V_{oc}$. This is based on the assumption that this single thiophene unit reduces conjugation with the acceptor unit compared with a fused CPDT due to larger dihedral angles, which may prevent the recombination. Therefore, in this study, a new series of dyes called **T-CPDT** (Fig. 1) was designed and synthesised *via* an addition of one thiophene unit in between the CPDT units and cyanoacrylic acid as shown in Fig. 1, aiming to improve $V_{oc}$, while retaining high $J_{sc}$. Their characteristic properties were determined by experimental and theoretical techniques, and the solar cell devices based on them were tested using both $I^-/I_3^-$ liquid electrolyte and 2,2′,7,7′-tetrakis(*N*,*N*-di-*p*-methoxyphenyl-amine)-9,9′-spirobifluorene (Spiro-OMeTAD) as a HTM.

## Results and discussion

### Synthesis

Scheme 1 presents the synthetic route which was used to synthesise the **T-CPDT** series for DSSC applications. The synthesis started with the alkylation of the CPDT unit with two hexyl

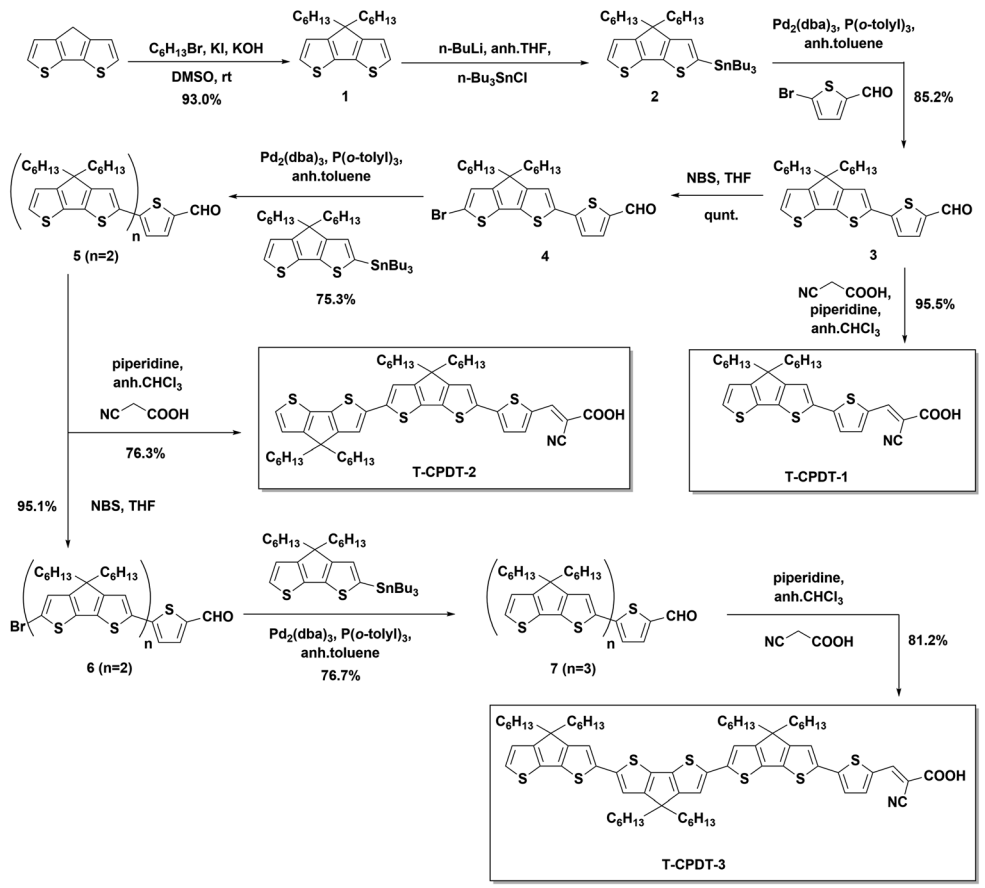


Scheme 1 The synthetic procedure of the T-CPDT series.

chains to give compound **1** which subsequently underwent stannylation to compound **2**. The Stille cross-coupling reaction was used to connect compound **2** with 5-bromothiophene-2-carbaldehyde to yield compound **3**. **T-CPDT-1** was synthesised *via* the Knoevenagel condensation catalysed by piperidine of compound **3** with 2-cyanoacetic acid. It was found that there are two isomers, (*E*)- and (*Z*)- of **T-CPDT-1** in which the (*E*)-isomer is the major product with approximately 84 : 16 of (*E*) : (*Z*) determined by $^1$H NMR as shown in Fig. S2†. The separation between these two isomers was difficult but partially possible as the (*E*)-isomer was eluted before the (*Z*)-isomer by conventional column chromatography as seen in Fig. S2,† where 97% purity of the (*E*)-isomer was obtained. However, there is some part of the mixture that cannot be purified and ends up being eluted as the mixture. By performing the dry column vacuum chromatography (DCVC) technique,[16] the purification is facilitated, but separation of the mixture is not improved. To synthesise compound **5**, compound **3** was brominated to give compound **4**, which subsequently reacted with compound **2** *via* the Stille cross-coupling reaction. Compound **5** was used as a starting material to synthesise **T-CPDT-2** by the Knoevenagel condensation, while in a separate reaction, the compound underwent the bromination reaction to give compound **6**. The Stille cross-coupling reaction between compound **6** and compound **2** gave compound **7** which was followed by the Knoevenagel condensation to yield the final dye, **T-CPDT-3**. As opposed to **T-CPDT-1**, there is no observation of two isomers in either **T-CPDT-2** or **T-CPDT-3**: only the (*E*)-isomer was observed in both products measured by $^1$H NMR.

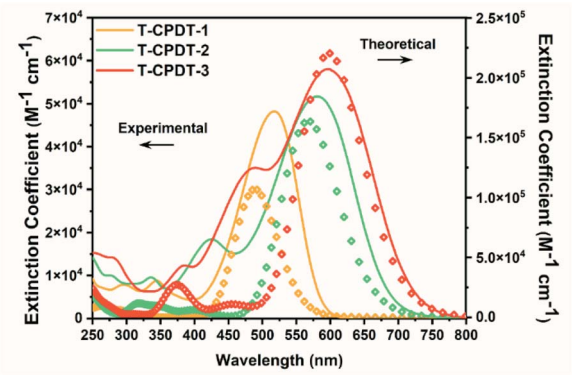


Fig. 2 UV-Vis spectra of the T-CPDT series (solid lines) in DCM together with theoretical absorption spectra (dots) with a FWHM of 3000 cm$^{-1}$ in DCM (PCM solvation model).

## Optical and electrochemical properties

Fig. 2 shows the UV-Vis absorption spectra of the **T-CPDT** series in DCM solution. A Beer–Lambert plot was applied to determine the extinction coefficients of each dye, and they all show linear behaviour over measured concentrations in the range of 5–20 μM, confirming no aggregation. Their corresponding optical properties are summarised in Table 1. These absorption spectra arise from intramolecular charge transfer (ICT) from the CPDT unit(s) to the cyanoacrylic acid group. From Fig. 2, it is clearly seen that the extension of the number of CPDT units leads to a bathochromic shift and higher extinction coefficient from **T-CPDT-1** to **T-CPDT-3**. Adding one CPDT unit on **T-CPDT-1** to form **T-CPDT-2** causes a large bathochromic shift (63 nm, 2093 cm$^{-1}$), while **T-CPDT-3** shows a slight bathochromic shift compared to **T-CPDT-2** (15 nm, 433 cm$^{-1}$). The colour of the corresponding dye solution in DCM is pink, purple, and dark blue for **T-CPDT-1**, **T-CPDT-2** and **T-CPDT-3**, respectively. Their optical gaps were calculated by extrapolation of the low-energy onset of their absorption peaks and are listed in Table 1. The additional thiophene unit also results in a further bathochromic shift when the **T-CPDT** dyes are compared to the analogous dyes in the **CPDT** series (Table 1). This is because the extra thiophene unit provides more conjugation; hence, the optical gap of the **T-CPDT** series is further reduced. However, as shown in Table 1, the extra thiophene unit reduces the extinction coefficient of the **T-CPDT** series, compared to the **CPDT** series. This might be due to the extra thiophene unit causing an overall larger dihedral angle in the **T-CPDT** series. Similar to the **CPDT** series, the coplanar CPDT unit(s) in the **T-CPDT** series results in a bathochromic shift and higher extinction coefficient than those in **5T**.

Cyclic voltammetry and square-wave voltammetry were carried out to estimate oxidation and reduction potentials and electrochemical reversibility of the **T-CPDT** series. HOMO and

Table 1 Photophysical and electrochemical properties of the T-CPDT series, CPDT-series and 5T

| Dye | $\lambda_{max}$[a] (nm), $\varepsilon$ (M$^{-1}$ cm$^{-1}$) | $E_{gap}^{opt}$[b] (eV) | $E_{ox}$ *vs.* NHE[c] (V) | $E_{red}$ *vs.* NHE[c] (V) | $E_{HOMO}$[d] (eV) | $E_{LUMO}$[e] (eV) | $E_{ox}^{*}$[f] (V) |
|---|---|---|---|---|---|---|---|
| **T-CPDT-1** | 518, 48 000 | 2.14 | 1.18 | −1.42 | −5.37 | −2.83 | −0.96 |
| **T-CPDT-2** | 581, 53 000 | 1.83 | 0.81 | −1.39 | −4.85 | −2.86 | −1.02 |
| **T-CPDT-3** | 596, 58 000 | 1.76 | 0.66 | −1.35 | −4.64 | −2.90 | −1.10 |
| **CPDT-1** | 456, 49000[g] | 2.43 | 1.46[g] | −1.54[g] | −5.76 | −2.71 | −0.97 |
| **CPDT-2** | 546, 54000[g] | 1.94 | 0.89[g] | −1.48[g] | −4.96 | −2.77 | −1.05 |
| **CPDT-3** | 585, 74000[g] | 1.77 | 0.71[g] | −1.44[g] | −4.71 | −2.81 | −1.06 |
| **5T** | 478, 39000[g] | 2.15 | 1.08[g] | −1.29[g] | −5.23 | −2.96 | −1.07 |

[a] Absorption spectra were obtained in DCM. [b] The optical energy gaps of the **T-CPDT** and the **CPDT** series were estimated by the onset of the corresponding dye's absorption spectrum. [c] Potentials were measured in DCM with 0.3 M $TBAPF_6$ as a supporting electrolyte *versus* Fc/Fc$^+$ and were converted to be against NHE by addition of 0.63 V.[17] [d] $E_{HOMO}$ energy was calculated from the equation of $-1.4(E_{ox}$ *vs.* Fc/Fc$^+) - 4.6$ (eV).[18] [e] $E_{LUMO}$ energy was estimated from the equation of $-4.88 - (E_{red}$ *vs.* Fc/Fc$^+)$ (eV).[19] [f] Excited state oxidation potential ($E_{ox}^{*}$) was calculated from $E_{ox} - E_{gap}^{opt}$. [g] The data were taken from ref. 15, except for $E_{gap}^{opt}$, $E_{HOMO}$, $E_{LUMO}$ and $E_{ox}^{*}$.

 

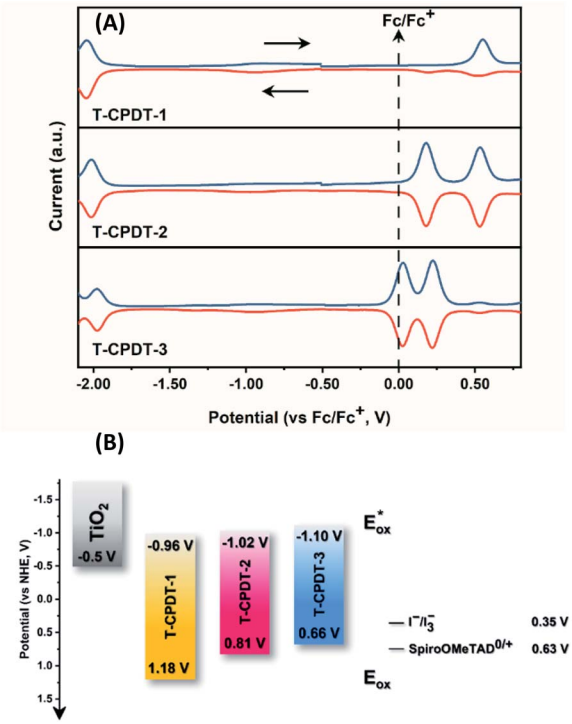


Fig. 3 (A) Square-wave voltammograms of the T-CPDT series in DCM and (B) energy alignment of the T-CPDT series in comparison with $TiO_2$ and commonly used electrolytes (the redox potential values were taken from ref. 20 and 21).

LUMO energies were calculated based on oxidation and reduction potentials, respectively. The results are tabulated in Table 1. The cyclic voltammogram of **T-CPDT-1** (Fig. S3†) shows that the oxidation process of **T-CPDT-1** is not fully chemically or electrochemically reversible within the time scale of electrochemical measurement. In contrast, **T-CPDT-2** and **T-CPDT-3** exhibit two reversible oxidation processes as shown in Fig. S3†. For the reduction processes as shown in the square-wave voltammograms (Fig. 3A), **T-CPDT-1** to **T-CPDT-3** all show a reversible reduction process. Fig. 3A also illustrates that adding more CPDT units shifts the oxidation potential to a less positive potential from **T-CPDT-1** to **T-CPDT-3**. Furthermore, **T-CPDT-3** undergoes further oxidation at a smaller additional potential than **T-CPDT-2**. On the other hand, more CPDT units do not affect the reduction potentials much, which indicates that the cyanoacrylic acid moiety determines the reduction processes. When compared to the **CPDT** series, the additional thiophene unit between CPDT and cyanoacrylic acid leads to even less positive oxidation potentials and slightly less negative reduction potentials as shown in Table 1.

Fig. 3B represents the energy diagram of the **T-CPDT** series along with a typical value of the conduction band (CB) potential of $TiO_2$ and redox potentials of the redox couples for the DSSCs used here. All the oxidation potentials of the **T-CPDT** series are more positive than the standard redox potential of $I^-/I_3^-$ electrolyte. This suggests sufficient dye regeneration. However, **T-CPDT-3** has a slightly more positive oxidation potential ($E_{ox}$) than that of Spiro-OMeTAD (0.63 V *vs.* NHE[21]), which indicates that dye regeneration might be slow when used in a solid-state based device with this HTM. Their excited-state oxidation potentials ($E^*_{ox}$) are more negative than the CB edge ($E_{CB}$) potential of $TiO_2$ (−0.5 V *vs.* NHE[20]), confirming sufficient driving force for electron injection from the excited dyes to the CB of $TiO_2$.

## Computational study

To gain insight into the frontier molecular orbitals of the **T-CPDT** series, DFT calculations were performed to optimise the dye geometry and their electron distribution. Fig. 4 shows the orbital distribution and electronic energy levels of the **T-CDPT** series in the DCM solvation model. The HOMO (highest occupied molecular orbital) of all molecules is mainly delocalised over the CPDT units. In contrast, the LUMO (lowest unoccupied molecular orbital) is shifted toward the cyanoacrylic acid group with some character on the additional thiophene unit. Thus, these computational results support the electrochemical results in terms of the relationship between oxidation and reduction potentials and HOMO and LUMO, respectively. Moreover, the calculations show a larger extent of separation between the HOMO and LUMO when more CPDT units are present in the structure. Time-dependent DFT (TDDFT) calculations were carried out to investigate the electronic transitions, and the results are shown in Fig. 2 and Table 2. The calculated electronic transitions correspond to those of the experimental ones: more CPDT units lead to a bathochromic shift and higher extinction coefficient. As shown in Table 2, the % MO contributions of the most intense transition obtained from the calculations with corresponding oscillator strengths ($f$) show that the transition character from the HOMO to the LUMO is predominant. When the molecule has greater conjugation, the

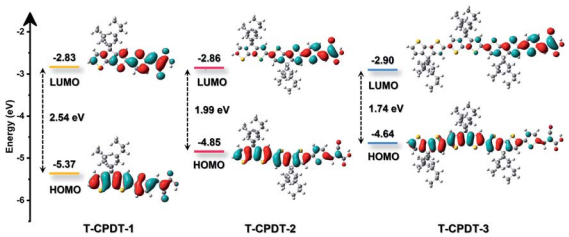


Fig. 4 The frontier molecular orbitals of the T-CPDT series with energy levels.

Table 2 Summary of corresponding calculations results from TDDFT

| Dye | $\lambda_{max}$ (nm) | % MO contribution | $f$ |
|---|---|---|---|
| **T-CPDT-1** | 491 | HOMO to LUMO (92%) | 1.47 |
| **T-CPDT-2** | 569 | HOMO to LUMO (79%) | 2.62 |
| **T-CPDT-3** | 599 | HOMO to LUMO (61%)<br>HOMO-1 to LUMO (17%)<br>HOMO to LUMO+1 (13%) | 3.04 |

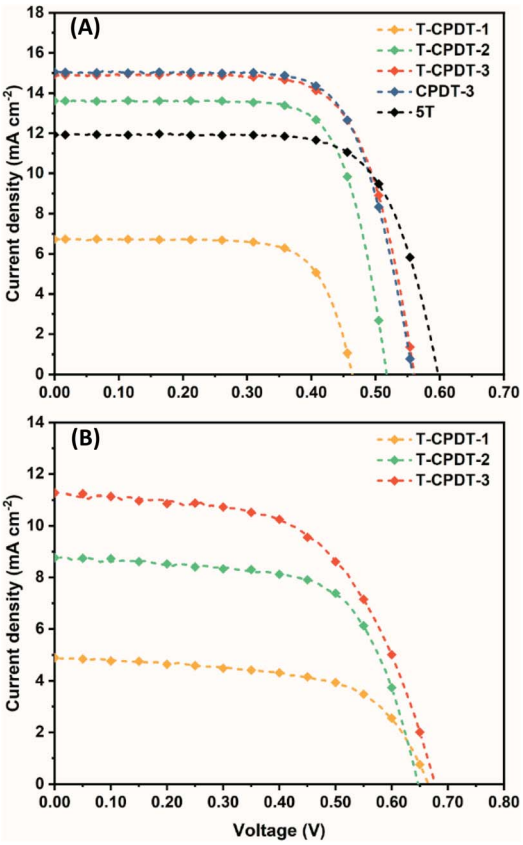


Fig. 5 *J–V* curves of (A) liquid devices with the T-CPDT series, CPDT-3 and 5T, and (B) solid-state devices with the T-CPDT series measured using an AM 1.5G solar simulator (illumination intensity of 100 mW $cm^{-2}$).

involvement of the HOMO-1 and LUMO+1 becomes a larger contribution as seen in **T-CPDT-3**. Regarding the oscillator strength, its value increases along with the length of CPDT units, indicating higher probability of the transition.

### Photovoltaic performances

The photovoltaic performances of the **T-CPDT** series were examined in both liquid ($I^-/I_3^-$) and solid-state (Spiro-OMeTAD as the HTM) DSSCs. For liquid-based devices with the **T-CPDT** series only, the corresponding current–voltage (*J–V*) curves of the best devices are shown in Fig. 5A, and the results are tabulated in Table 3. From the results, it is clearly seen that the device with **T-CPDT-3** achieved the highest power conversion efficiency (PCE) of 5.88%, followed by **T-CDPT-2** with a PCE of 5.19% and **T-CPDT-1** with a PCE of 2.27%, respectively. The higher $J_{sc}$ and $V_{oc}$ from **T-CPDT-3** than those of **T-CPDT-2** and **T-CDPT-1** are the main reasons for the higher PCE for **T-CPDT-3** than the others. For the ssDSSCs with **T-CPDT**, the corresponding *J–V* curves of the best devices are shown in Fig. 5B, and the results are tabulated in Table 3. Similarly, **T-CPDT-3** achieved the highest PCE mainly due to higher $J_{sc}$ and $V_{oc}$. The $J_{sc}$ from the best solid-state device based on **T-CPDT-3** (11.27 mA $cm^{-2}$) is astonishingly high with the $TiO_2$ film thickness less than 1 μm (0.96 μm in this work). It is worth mentioning that the optimised $TiO_2$ film thickness in ssDSSCs is generally around 2 μm.[22,23] Although **T-CPDT-3** achieved higher $J_{sc}$ and $V_{oc}$, it suffers from low ff, which is likely due to the low dye regeneration driving force as suggested in Fig. 5B. It is also worth mentioning that **T-CPDT-3** as suggested in Fig. 5B exhibits a good performance (4.38% from the best cell) among ssDSSCs with Spiro-OMeTAD and the same additives (Table S1†). Recently, there has been some interesting work on new dyes (**S5**[24] and **AQ310**[25]) for ssDSSCs with Spiro-OMeTAD, which show outstanding PCEs (around 8%). They both exhibit comparable $J_{sc}$ (with a 2.2 μm $TiO_2$ layer) to **T-CPDT-3** but higher $V_{oc}$ and ff. This implies that the improvement in $V_{oc}$ and ff for **T-CPDT-3** is needed in order to achieve higher PCE.

The improvement of $J_{sc}$ with increasing the number of CPDT units can be explained in terms of larger conjugation leading to a higher extinction coefficient and an expansion of the absorption peak towards 800 nm. The IPCE can be explained in terms of injection efficiency ($\varphi_{inj}$), charge collection efficiency ($\eta_{col}$), light harvesting efficiency (LHE($\lambda$)), and dye regeneration efficiency ($\varphi_{reg}$) as shown in eqn (1):[26]

$$\mathrm{IPCE} = \mathrm{LHE}(\lambda) \times \varphi_{inj} \times \varphi_{reg} \times \eta_{col} \quad (1)$$

Considering the driving force for charge injection by the difference between their $E_{ox}^{*}$ and CB of $TiO_2$, they are greater than 0.2 V, which indicates fast injection rate considered to be nearly unity.[27] Moreover, sufficient driving force for dye regeneration is guaranteed as mentioned above. By comparing their

Table 3 Photovoltaic parameters of solar cells with the T-CPDT series, CPDT and 5T under illumination of AM 1.5G (100 mW $cm^{-2}$)[a]

| Dye | Electrolyte | $J_{sc}$ (mA $cm^{-2}$) | $V_{oc}$ (V) | ff | PCE (%) | Dye loading (mol $cm^{-2}$) |
|---|---|---|---|---|---|---|
| **T-CPDT-1** | $I^-/I_3^-$ | 6.72 (6.55 ± 0.13) | 0.46 (0.47 ± 0.03) | 0.73 (0.71 ± 0.02) | 2.27 (2.18 ± 0.08) | $1.45 \times 10^{-7}$ |
| **T-CPDT-2** | $I^-/I_3^-$ | 13.61 (13.49 ± 0.94) | 0.52 (0.51 ± 0.01) | 0.73 (0.71 ± 0.02) | 5.19 (4.93 ± 0.18) | $1.70 \times 10^{-7}$ |
| **T-CPDT-3** | $I^-/I_3^-$ | 14.90 (14.88 ± 0.88) | 0.56 (0.55 ± 0.01) | 0.71 (0.68 ± 0.02) | 5.88 (5.60 ± 0.27) | $1.88 \times 10^{-7}$ |
| **CPDT-3** | $I^-/I_3^-$ | 15.07 (14.37 ± 0.53) | 0.56 (0.56 ± 0.01) | 0.71 (0.68 ± 0.05) | 5.95 (5.53 ± 0.35) | $1.85 \times 10^{-7}$ |
| **5T** | $I^-/I_3^-$ | 11.92 (11.65 ± 0.22) | 0.60 (0.59 ± 0.01) | 0.71 (0.73 ± 0.01) | 5.06 (5.03 ± 0.05) | $2.35 \times 10^{-7}$ |
| **T-CPDT-1** | Spiro | 4.90 (4.34 ± 0.30) | 0.66 (0.65 ± 0.01) | 0.61 (0.61 ± 0.01) | 1.98 (1.72 ± 0.13) | — |
| **T-CPDT-2** | Spiro | 8.82 (8.13 ± 0.69) | 0.65 (0.65 ± 0.01) | 0.65 (0.64 ± 0.02) | 3.70 (3.36 ± 0.29) | — |
| **T-CPDT-3** | Spiro | 11.27 (10.17 ± 0.76) | 0.68 (0.67 ± 0.01) | 0.58 (0.53 ± 0.07) | 4.38 (3.59 ± 0.45) | — |

[a] The average results in brackets were calculated from 4 individual cells for $I^-/I_3^-$ electrolyte and from 8 individual cells for the Spiro-OMeTAD HTM.

 

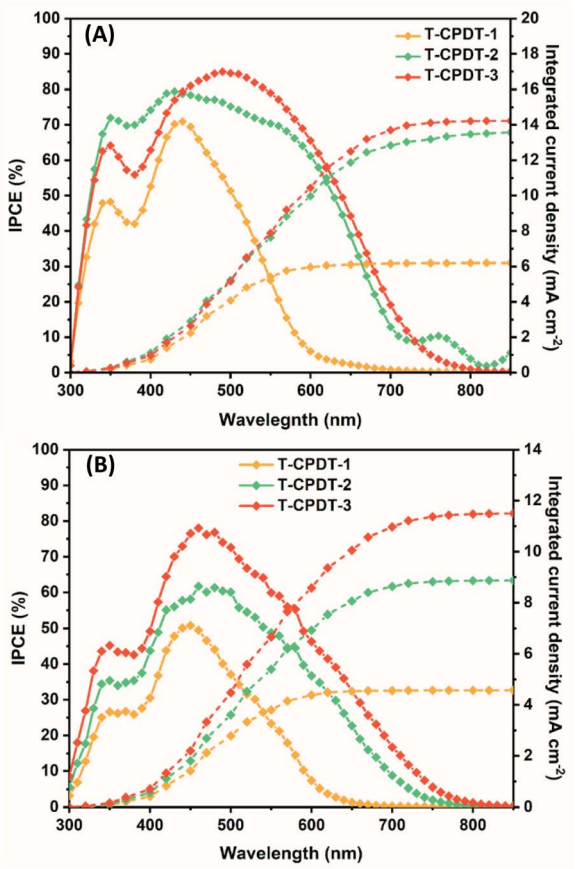


Fig. 6 IPCE spectra of the T-CPDT series from (A) liquid devices and (B) solid-state devices.

absorption spectra shown in Fig. 2, it suggests that the LHE($\lambda$) has an influence on the improvement of $J_{sc}$. As seen in Fig. 6A and B, **T-CPDT-3** shows the broadest IPCE over a range of 400–700 nm and an extension to around 800 nm with a maximum IPCE of approximately 85% for the liquid-based device and 80% for the solid-state device. Although **T-CPDT-2** exhibits high IPCE in the range of 300–400 nm and broad IPCE over almost the same range as **T-CPDT-3** for liquid-based devices, its maximum IPCE is around 80%, which is lower than that of **T-CPDT-3**. For solid-state devices, **T-CPDT-2** clearly shows lower IPCE than that of **T-CPDT-3.** A narrow range and small IPCE values are observed for **T-CPDT-1** in both types of devices, which explains why it attained the smallest $J_{sc}$. The integrated $J_{sc}$ values from their corresponding IPCE are in good agreement with the experimental results from *J–V* measurement.

To probe the postulation that the additional thiophene unit in the **T-CPDT** series, compared to **CPDT-3** and **5T**, would improve $V_{oc}$, devices with **T-CPDT**, **CPDT-3** and **5T** were fabricated for liquid-based devices. The results are tabulated in Table 3. The devices with **T-CPDT-3** and **CPDT-3** achieved comparable PCE and $J_{sc}$ while **5T** had lower $J_{sc}$ compared to them. The lower $J_{sc}$ in **5T** originates from a lower absorption coefficient (Table 1) than those of **T-CPDT-3** and **CPDT-3**, hence, lower light harvesting capability under the same device conditions *i.e.*, the same thickness of $TiO_2$. In contrast to the PCE and $J_{sc}$ results, **5T** achieved the highest $V_{oc}$, while **T-CPDT-3** and **CPDT-3** showed approximately the same $V_{oc}$, followed by **T-CPDT-2** and **T-CPDT-1**, respectively. Therefore, the additional thiophene did not help to improve $V_{oc}$. However, the extra thiophene unit did not lead to detrimental performances as evidenced by the improved overall performance of **T-CPDT-1** and the improved $J_{sc}$ of **T-CPDT-2** when compared to **CPDT-1**[15] and **CPDT-2**,[15] respectively.

### Electrochemical impedance spectroscopy (EIS)

According to the performance results, differences in $V_{oc}$ within the **T-CPDT** series and among the **T-CPDT**, **CPDT-3** and **5T** were observed. In order to clarify these differences, impedance spectroscopy (EIS) measurements on liquid-based devices were performed in the frequency range between 0.1 MHz and 0.05 Hz under LED illumination at various forward biases. The EIS spectra were fitted using the transmission line model,[28] and the equivalent circuit is shown in Fig. S4†. The EIS spectra exhibit a typical DSSC feature where the Pt/electrolyte interface charge transfer and $TiO_2$/dye/electrolyte interface are represented by the first semicircle at high frequencies and the middle semicircle at intermediate frequencies, respectively, as shown in Fig. 7.[29]

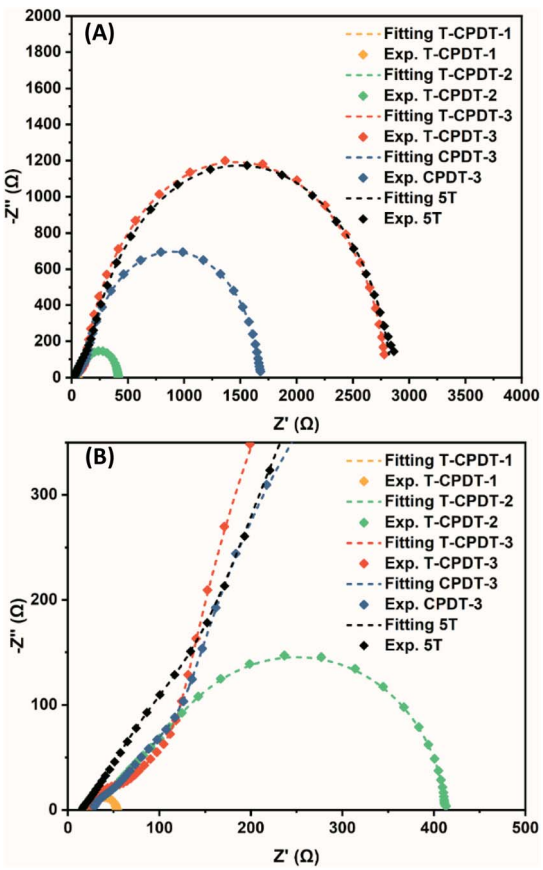


Fig. 7 (A) Nyquist plot of the T-CPDT series, CPDT-3 and 5T, and (B) enlarged Nyquist plot.

Fitting of the EIS spectra enabled chemical capacitance ($C_\mu$), transport resistance ($R_t$) and charge recombination resistance ($R_{rec}$) at the $TiO_2$/dye/electrolyte interface to be extracted. Since a constant phase element (CPE) is often used in EIS fitting, the equivalent capacitance of the CPE, hereafter $C_\mu$, is calculated by eqn (2):[29,30]

$$C_\mu = \frac{(RQ)^{1/m}}{R} \quad (2)$$

where $Q$ is the CPE prefactor, $m$ is the CPE index and $R$ is the resistor parallel to the corresponding CPE. Fig. 8A shows $C_\mu$ as a function of voltage, and it clearly shows that $C_\mu$ increases with increasing voltage as depicted in eqn (3):[31]

$$C_\mu = L(1 - p)\alpha\frac{q^2 N_t}{k_B T}\exp\left[\frac{\alpha(E_{redox} - E_{CB})}{k_B T}\right]\exp\left[\frac{\alpha q V}{k_B T}\right]$$

$$C_\mu = C_0\exp\left[\frac{\alpha q V}{k_B T}\right] \quad (3)$$

where $L$ is the film thickness, $p$ is the porosity of the film, $N_t$ is the total number of trap states below the conduction band (CB) and $\alpha$ is the trap distribution parameter. As shown in Fig. 8A, a significantly different trend in $C_\mu$ is observed from **T-CPDT-1** with respect to other dyes which all have similar slopes. This suggests that the device with **T-CPDT-1** has a different $\alpha$ with respect to other dyes: 0.44, 0.29, 0.30, 0.31, and 0.26 for **T-CPDT-1**, **T-CPDT-2**, **T-CPDT-3**, **CPDT-3** and **5T**, respectively. Assuming that the film thickness and porosity are the same across the devices, $C_\mu$ also depends on $N_t$ and $E_{CB}$ through $C_0$ as shown in eqn (3). Thus, Fig. 8A also shows a displacement of the CB produced by different dyes (**T-CPDT-2**, **T-CPDT-3**, **CPDT-3** and **5T**) with the same electrolyte. The positive shift towards higher voltage indicates that the conduction band edge ($E_{CB}$) shifts upwards.[29] Therefore, the trend in $C_\mu$ in Fig. 8A indicates that the $E_{CB}$ of **5T** > **CPDT-3** > **T-CPDT-3** > **T-CPDT-2**.

The dependence of electron transport resistance ($R_t$) on voltage can be explained *via* eqn (4)[28,32] shown below:

$$R_t = R_{t0}\exp\left[-\frac{q}{k_B T}\left(V + \frac{E_{F,redox} - E_{CB}}{k_B T}\right)\right] \quad (4)$$

where $R_{t0}$ is the preexponential factor and considered as a constant across the series given that the geometry of $TiO_2$ is similar,[28] and $E_{F,redox}$ is the redox potential of the redox couple. Eqn (4) shows that $R_t$ decreases exponentially with increasing voltage as seen in Fig. 8B. Provided that $E_{F,redox}$ remains unchanged, fitting $R_t$ as a function of voltage provides information about $E_{CB}$ relative to $E_{F,redox}$. In Fig. 8B, a positive shift indicates the displacement $E_{CB}$ towards a higher level as suggested in eqn (4).[32] As shown in Fig. 8B, there is a positive shift around 10 mV from **T-CPDT-3** to **CPDT-3** and around 30 mV from **T-CPDT-3** to **5T**, whereas no significant shift is observed from **T-CPDT-2** to **T-CPDT-3**. As a result, the trend in the $E_{CB}$ shift from the $R_t$ results is **5T** > **CPDT-3** > **T-CPDT-3** ≈ **T-CPDT-2**, which agrees quite well with the results from the $C_\mu$ and voltage curve (Fig. 8A). Note that the impedance spectra of **T-CPDT-2** exhibit a Gerischer impedance at low potentials in which $R_t$ cannot be extracted unambiguously,[29,33] and **T-CPDT-1** does not show a clear trend in electron transport (Fig. 7B); therefore, it is not considered in this result. Although **CPDT-3** shows higher $E_{CB}$ than **T-CPDT-3**, the *J*–*V* curve results show that they have the same $V_{oc}$.

The differences in $E_{CB}$ can originate from the dipole moment of the dye as shown in Fig. 9. The dipole moment of dyes can affect the energetics of the $TiO_2$ electrode according to eqn (5):[34]

$$\Delta E_{CB} = -\frac{q\vec{\mu}_{normal}\gamma}{\varepsilon_0\varepsilon} \quad (5)$$

where $\Delta E_{CB}$ is the shift in the $TiO_2$ CB, $\vec{\mu}_{normal}$ is the dipole moment component of individual molecules perpendicular to the surface, $\gamma$ is the dye surface concentration, and $\varepsilon_0$ and $\varepsilon$ are the dielectric constant of the monolayer and the permittivity of the vacuum, respectively. Assuming that the orientation of the dyes is perpendicular to the $TiO_2$ surface by using the cyanoacrylic acid group to bind on the surface, $\vec{\mu}_{normal}$ can be represented by $\mu_{total}$ in which it points outwards from the $TiO_2$ surface as shown in Fig. 9. This direction of the negative dipole moment is known to induce an upward shift of $E_{CB}$ as it aligns the electron-rich end of the molecule on the $TiO_2$ surface.[34] Thus, the larger the magnitude of $\vec{\mu}_{normal}$, the more negative the shift (electrochemical scale) in the $TiO_2$ CB, leading to higher $V_{oc}$. As shown by the results in Fig. 9, the largest $\mu_{total}$ is

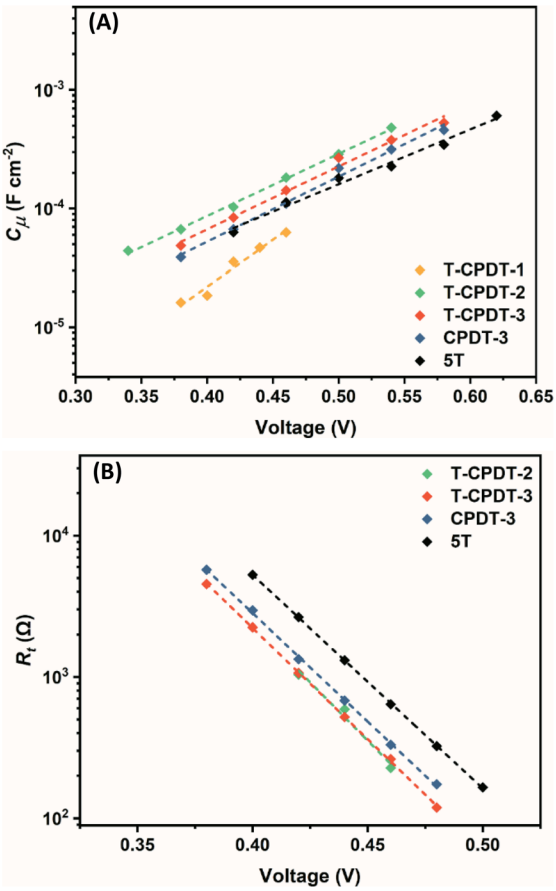


Fig. 8 (A) Chemical capacitance ($C_\mu$) and (B) transport resistance ($R_t$) against voltage.

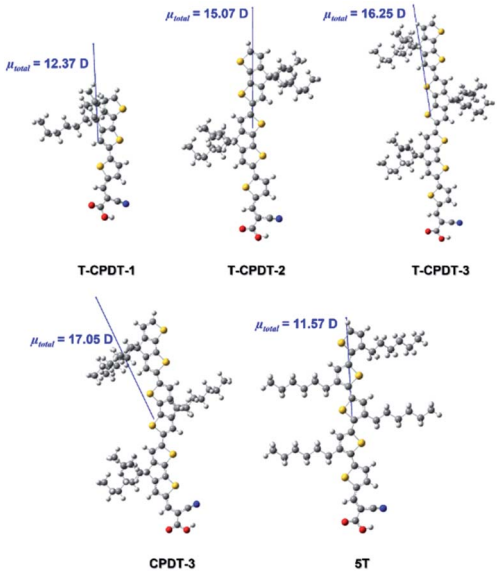


Fig. 9 The total dipole moment from the T-CPDT series, CPDT-3 and 5T calculated by DFT with DCM (PCM solvation model).

seen from **CPDT-3** > **T-CPDT-3** > **T-CPDT-2** > **T-CPDT-1** > **5T**. Therefore, the $\mu_{total}$ results seem to agree well with the trend in $C_\mu$, except for **5T** which has the lowest $\mu_{total}$, but the highest $E_{CB}$ as mentioned above. However, the $\Delta E_{CB}$ also depends on $\gamma$ as suggested in eqn (5). The dye desorption results indicate that the dye loading amount of **5T** is the highest as shown in Table 3. This may contribute to an overall greater upward shift of $E_{CB}$ in **5T**. It is noteworthy that the dye orientation may not be perfectly perpendicular to the $TiO_2$ surface in the real situation. This can also cause some variation in the $E_{CB}$ shift according to eqn (5). Notwithstanding this caveat, the dipole moment and dye coverage results seem to be important parameters determining the trend in the $E_{CB}$ shift.

The trends shown in the conduction band energy (Fig. 8A and B) contribute significantly to the different $V_{oc}$ across the devices that possess similar $\alpha$ (**T-CPDT-2**, **T-CPDT-3**, **CPDT-3** and **5T**); however, for a complete picture, it may be necessary to also analyse the electron recombination process at the $TiO_2$/dye/electrolyte interface. In terms of the electron recombination process, the recombination resistance ($R_{rec}$) and electron lifetime ($\tau_n$) can be used to quantify the recombination between electrons in $TiO_2$ and the redox couple in the electrolyte.[35] While $R_{rec}$ can be extracted from fitting the impedance spectrum, $\tau_n$ can be determined by the relationship between $C_\mu$ and $R_{rec}$ as shown in eqn (6):[29]

$$\tau_n = C_\mu R_{rec} \quad (6)$$

To decouple the contribution of voltage to the electron recombination in different devices, fitting $R_{rec}$ and $\tau_n$ as a function of electron density ($n$) is used, and $n$ can be determined *via* eqn (7):[36]

$$n = \frac{C_\mu k_B T}{q^2 L \alpha} \quad (7)$$

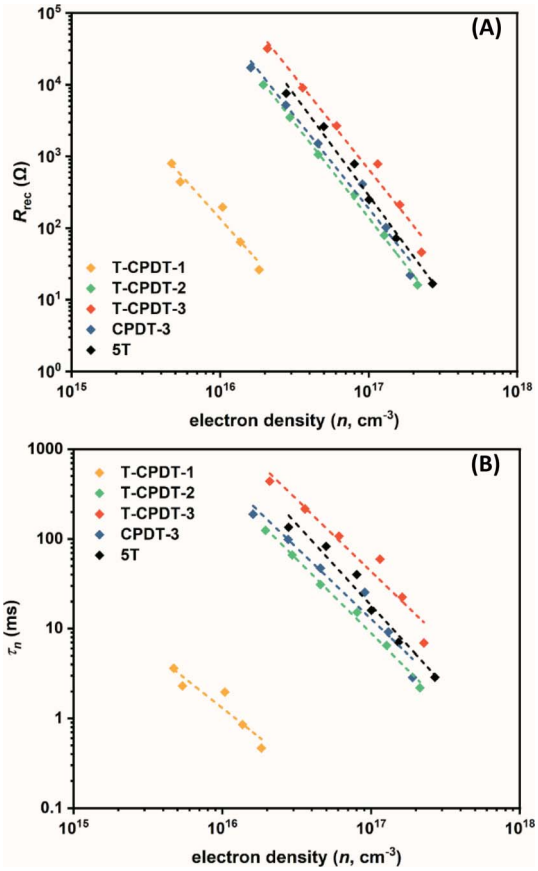


Fig. 10 (A) Recombination resistance ($R_{rec}$) and (B) electron lifetime ($\tau_n$) as a function of electron density ($n$).

Fig. 10A and B illustrate, respectively, the $R_{rec}$ and $\tau_n$ as a function of electron density, in which their values decrease exponentially with increasing electron density. From the $R_{rec}$ results in Fig. 10A, it can be seen that **T-CPDT-3** has the largest $R_{rec}$ followed by **5T**, **CPDT-3**, **T-CPDT-2** and **T-CPDT-1**. In line with $R_{rec}$, the same trend is also observed in $\tau_n$ as shown in Fig. 10B. This suggests that the electron recombination with the redox electrolyte in the device with **T-CPDT-3** is impeded most effectively among the studied dyes, hence, the longest $\tau_n$.

To rationalise the electron recombination results, it can be linked to the dye structure. In the dye design, long alkyl chains are normally introduced into the structure to prevent aggregation and electron recombination.[11–13] Due to the hydrophobic properties of long alkyl chains, they can prevent hydrophilic redox ions, such as $I_3^-$, from approaching the $TiO_2$ surface, leading to a decrease in the $I_3^-$ concentration near the $TiO_2$ surface, hence, suppression of electron recombination.[35,37] As shown in Fig. 1, **T-CPDT-3** has 6 hexyl chains alternating in the opposite orientation, whereas **T-CPDT-2** and **T-CPDT-1** have 4 and 2 hexyl chains, respectively. As a result, **T-CPDT-3** can prevent the electron recombination more effectively among the **T-CPDT** series, contributing to the enhancement of $V_{oc}$ from **T-CPDT-1** to **T-CPDT-3**. Interestingly, the addition of the thiophene unit to **CPDT-3** yielding **T-CPDT-3** increases $R_{rec}$ and $\tau_n$, which is not normal as the longer π-conjugation is likely to

facilitate the electron recombination.[38,39] This might be attributed to the extra thiophene in **T-CPDT-3** mitigating the electron recombination by separating the last CPDT unit and cyanoacrylic acid group, which further decreases the $I_3^-$ concentration near the $TiO_2$ surface. In addition, the overall larger dihedral angles of **T-CPDT-3** with respect to **CPDT-3** (from the UV-Vis results) may also contribute to slower electron recombination kinetics. As a result, the electron recombination is less likely to occur. The same rationale of the number of alkyl chains can also be used to explain the difference in $R_{rec}$ and $\tau_n$ between **T-CPDT-3** and **5T** as **T-CPDT-3** has more hexyl chains than **5T**, hence, higher $R_{rec}$ and $\tau_n$ in **T-CPDT-3**. Although **T-CPDT-2** and **5T** have the same number of hexyl chains, there is a difference in recombination kinetics between them. This might be attributed to the dye coverage results shown in Table 3, revealing that there is more **5T** on the $TiO_2$ surface, compared to **T-CPDT-2**.

According to the EIS results, one can summarise the trend in different $V_{oc}$ with the extra thiophene unit in the **T-CPDT** series, **CPDT-3** and **5T** in terms of the $E_{CB}$ shift and electron recombination kinetics. Among the **T-CPDT** series, it is clear that **T-CPDT-1** and **T-CPDT-2** show faster recombination kinetics, and also lower $E_{CB}$ in **T-CPDT-2**, compared with **T-CPDT-3**, **CPDT-3** and **5T**. Thus, they achieved lower $V_{oc}$ compared to **T-CPDT-3**, **CPDT-3** and **5T**. Comparing **T-CPDT-3** and **CPDT-3**, the former has lower $E_{CB}$, but this is compensated by slower electron recombination kinetics attributed to effectively blocking $I_3^-$ from approaching the $TiO_2$ surface, which eventually leads to similar $V_{oc}$. Comparing **T-CPDT-3** and **5T**, the $E_{CB}$ upwards shift in **5T** due to larger dye coverage is more pronounced than the slower electron recombination kinetics in **T-CPDT-3**; hence, the highest $V_{oc}$ is in the device with **5T**. For $V_{oc}$ trends in ssDSSCs, we believe that the study of EIS among the **T-CPDT** series in liquid-based devices can also be applied to solid-state devices.

## Conclusions

A new series of dyes called **T-CPDT** (denoted as **T-CPDT-1**, **T-CPDT-2** and **T-CPDT-3**) was designed and synthesised, using linked CPDT units and adding a thiophene unit between CPDT and cyanoacrylic acid units. The optical properties of the **T-CPDT** series show that the increase in CPDT units leads to a bathochromic shift. The electrochemical characterisation reveals that the oxidation potential becomes less positive with increasing CPDT units. When compared to the **CPDT** counterpart dyes without the added thiophene, the addition of thiophene causes a bathochromic shift and lower oxidation potential. The DSSC results based on the **T-CPDT** series with $I^-/I_3^-$ electrolyte and Spiro-OMeTAD as the HTM show that $J_{sc}$, $V_{oc}$ and PCE increase upon addition of CPDT units with the champion cell of **T-CPDT-3** achieving 5.88% and 4.38% for the $I^-/I_3^-$-based cell and solid-state cell, respectively. A comparison of the liquid-based DSSC with **CPDT-3** and **5T** was made under the same conditions. The devices with **T-CPDT-3** and **CPDT-3** show similar *J–V* results in all aspects, while the device with **5T** attains higher $V_{oc}$ but lower $J_{sc}$ and PCE than **T-CPDT-3**. The EIS results reveal that the additional thiophene unit leads to slower electron recombination kinetics which subsequently prolongs the electron lifetime in **T-CPDT-3**, compared to **CPDT-3**. However, the dipole moment of **T-CPDT-3** becomes lower with this extra thiophene, compared to **CPDT-3**. As a result, they give similar $V_{oc}$ attributed to compensation of these effects of the additional thiophene. The EIS results also show that although **5T** has faster electron recombination kinetics and a shorter electron lifetime than **T-CPDT-3**, more **5T** dye can be loaded on the $TiO_2$ surface, hence, a more upward shift in $E_{CB}$ for **5T**. The effect of this $E_{CB}$ shift is more pronounced than the slower electron recombination and longer electron lifetime in **T-CPDT-3**; thus, **5T** can achieve higher $V_{oc}$ than **T-CPDT-3**. Interestingly, **T-CPDT-3** can achieve outstanding $J_{sc}$ (11.27 mA $cm^{-2}$) in a solid-state device with the $TiO_2$ film thickness less than 1 micron. This implies that **T-CPDT-3** can be a promising dye for co-sensitisation with any dyes that have low current but high voltage, to complement their properties and achieve highly efficient solar cells.

## Author contributions

AJ: carried out and analysed most of the experimental work and initial manuscript drafting; XL: carried out the ssDSSC cell fabrication, testing and IPCE measurements for all devices; NR: supervision of most of the experimental work and manuscript review & editing; WW: supervision of the ssDSSC and IPCE experimental work and manuscript review.

## Conflicts of interest

There are no conflicts to declare.

## Acknowledgements

AJ would like to thank the Royal Government of Thailand through the Development and Promotion of Science and Technology Talents Project (DPST) for funding. WW gratefully thanks the National Natural Science Foundation of China (NFSC 22075083) for financial support.

## References

1 B. O'Regan and M. Grätzel, *Nature*, 1991, **353**, 737–740.
2 S. Zhang, X. Yang, Y. Numata and L. Han, *Energy Environ. Sci.*, 2013, **6**, 1443–1464.
3 A. Hagfeldt, G. Boschloo, L. Sun, L. Kloo and H. Pettersson, *Chem. Rev.*, 2010, **110**, 6595–6663.
4 B. Liu, B. Wang, R. Wang, L. Gao, S. Huo, Q. Liu, X. Li and W. Zhu, *J. Mater. Chem. A*, 2014, **2**, 804–812.
5 R. Grisorio, L. De Marco, R. Agosta, R. Iacobellis, R. Giannuzzi, M. Manca, P. Mastrorilli, G. Gigli and G. P. Suranna, *ChemSusChem*, 2014, **7**, 2659–2669.
6 Y. Tan, M. Liang, Z. Lu, Y. Zheng, X. Tong, Z. Sun and S. Xue, *Org. Lett.*, 2014, **16**, 3978–3981.
7 Y. Wu, W.-H. Zhu, S. M. Zakeeruddin and M. Grätzel, *ACS Appl. Mater. Interfaces*, 2015, **7**, 9307–9318.
8 C.-J. Tan, C.-S. Yang, Y.-C. Sheng, H. W. Amini and H.-H. G. Tsai, *J. Phys. Chem. C*, 2016, **120**, 21272–21284.

 

9 J. Zhang, Y.-H. Kan, H.-B. Li, Y. Geng, Y. Wu and Z.-M. Su, *Dyes Pigm.*, 2012, **95**, 313–321.
10 C.-G. Wu, W.-T. Shieh, C.-S. Yang, C.-J. Tan, C.-H. Chang, S.-C. Chen, C.-Y. Wu and H.-H. G. Tsai, *Dyes Pigm.*, 2013, **99**, 1091–1100.
11 Q. Chai, W. Li, J. Liu, Z. Geng, H. Tian and W. Zhu, *Sci. Rep.*, 2015, **5**, 11330.
12 X. Cheng, S. Sun, M. Liang, Y. Shi, Z. Sun and S. Xue, *Dyes Pigm.*, 2012, **92**, 1292–1299.
13 C. Baldoli, S. Bertuolo, E. Licandro, L. Viglianti, P. Mussini, G. Marotta, P. Salvatori, F. De Angelis, P. Manca, N. Manfredi and A. Abbotto, *Dyes Pigm.*, 2015, **121**, 351–362.
14 A. Abate, M. Planells, D. J. Hollman, S. D. Stranks, A. Petrozza, A. R. S. Kandada, Y. Vaynzof, S. K. Pathak, N. Robertson and H. J. Snaith, *Adv. Energy Mater.*, 2014, **4**, 1400166.
15 Y. Hu, A. Abate, Y. Cao, A. Ivaturi, S. M. Zakeeruddin, M. Grätzel and N. Robertson, *J. Phys. Chem. C*, 2016, **120**, 15027–15034.
16 D. S. Pedersen and C. Rosenbohm, *Synthesis*, 2001, **2001**, 2431–2434.
17 V. V Pavlishchuk and A. W. Addison, *Inorg. Chim. Acta*, 2000, **298**, 97–102.
18 B. W. D'Andrade, S. Datta, S. R. Forrest, P. Djurovich, E. Polikarpov and M. E. Thompson, *Org. Electron.*, 2005, **6**, 11–20.
19 M. Planells, A. Abate, H. J. Snaith and N. Robertson, *ACS Appl. Mater. Interfaces*, 2014, **6**, 17226–17235.
20 G. Boschloo, *Front. Chem.*, 2019, **7**, 77.
21 B. Xu, H. Tian, L. Lin, D. Qian, H. Chen, J. Zhang, N. Vlachopoulos, G. Boschloo, Y. Luo, F. Zhang, A. Hagfeldt and L. Sun, *Adv. Energy Mater.*, 2015, **5**, 1401185.
22 W. H. Nguyen, C. D. Bailie, J. Burschka, T. Moehl, M. Grätzel, M. D. McGehee and A. Sellinger, *Chem. Mater.*, 2013, **25**, 1519–1525.
23 I. Benesperi, H. Michaels and M. Freitag, *J. Mater. Chem. C*, 2018, **6**, 11903–11942.
24 Z. Shen, B. Xu, P. Liu, Y. Hu, Y. Yu, H. Ding, L. Kloo, J. Hua, L. Sun and H. Tian, *J. Mater. Chem. A*, 2017, **5**, 1242–1247.
25 X. Li, B. Xu, P. Liu, Y. Hu, L. Kloo, J. Hua, L. Sun and H. Tian, *J. Mater. Chem. A*, 2017, **5**, 3157–3166.
26 J.-M. Ji, H. Zhou, Y. K. Eom, C. H. Kim and H. K. Kim, *Adv. Energy Mater.*, 2020, **10**, 2000124.
27 Y. Xie, W. Wu, H. Zhu, J. Liu, W. Zhang, H. Tian and W.-H. Zhu, *Chem. Sci.*, 2016, **7**, 544–549.
28 F. Fabregat-Santiago, J. Bisquert, G. Garcia-Belmonte, G. Boschloo and A. Hagfeldt, *Sol. Energy Mater. Sol. Cells*, 2005, **87**, 117–131.
29 F. Fabregat-Santiago, G. Garcia-Belmonte, I. Mora-Seró and J. Bisquert, *Phys. Chem. Chem. Phys.*, 2011, **13**, 9083–9118.
30 A. Sacco, *Renewable Sustainable Energy Rev.*, 2017, **79**, 814–829.
31 S. R. Raga, E. M. Barea and F. Fabregat-Santiago, *J. Phys. Chem. Lett.*, 2012, **3**, 1629–1634.
32 Q. Wang, S. Ito, M. Grätzel, F. Fabregat-Santiago, I. Mora-Seró, J. Bisquert, T. Bessho and H. Imai, *J. Phys. Chem. B*, 2006, **110**, 25210–25221.
33 J. Bisquert, I. Mora-Sero and F. Fabregat-Santiago, *ChemElectroChem*, 2014, **1**, 289–296.
34 J. Preat, D. Jacquemin and E. A. Perpète, *Energy Environ. Sci.*, 2010, **3**, 891–904.
35 E. M. Barea and J. Bisquert, *Langmuir*, 2013, **29**, 8773–8781.
36 P. R. F. Barnes, K. Miettunen, X. Li, A. Y. Anderson, T. Bessho, M. Gratzel and B. C. O'Regan, *Adv. Mater.*, 2013, **25**, 1881–1922.
37 N. Koumura, Z.-S. Wang, S. Mori, M. Miyashita, E. Suzuki and K. Hara, *J. Am. Chem. Soc.*, 2006, **128**, 14256–14257.
38 T. Marinado, K. Nonomura, J. Nissfolk, M. K. Karlsson, D. P. Hagberg, L. Sun, S. Mori and A. Hagfeldt, *Langmuir*, 2010, **26**, 2592–2598.
39 S. Namuangruk, R. Fukuda, M. Ehara, J. Meeprasert, T. Khanasa, S. Morada, T. Kaewin, S. Jungsuttiwong, T. Sudyoadsuk and V. Promarak, *J. Phys. Chem. C*, 2012, **116**, 25653–25663.